

Influence of Si segregates on the structural evolution, mechanical properties, and high-temperature fracture toughness of Cr-Si-B_{2±z} coatings

L. Zauner^{1*}, R. Hahn¹, O. Hunold², J. Ramm², S. Kolozsvári³, P. Polcik³, and H. Riedl^{1,4}

¹ Christian Doppler Laboratory for Surface Engineering of high-performance Components, TU Wien, Austria

² Oerlikon Balzers, Oerlikon Surface Solutions AG, Liechtenstein

³ Plansee Composite Materials GmbH, Germany

⁴ Institute of Materials Science and Technology, TU Wien, Austria

*L.Z. Corresponding Author, Author 1

Christian Doppler Laboratory for Surface Engineering of high-performance Components, TU Wien
Getreidemarkt 9

1060 Wien, Austria

lukas.zauner@tuwien.ac.at

+4315880130820

ORCID-ID: 0000-0002-8373-6552

R.H. Author 2

rainer.hahn@tuwien.ac.at

O.H. Author 3

Oliver.Hunold@oerlikon.com

J.R. Author 4

juergen.ramm@oerlikon.com

S.K. Author 5

Szilard.Kolozsvari@plansee.com

P.P. Author 6

Peter.Polcik@plansee.com

H.R. Author 7

helmut.riedl@tuwien.ac.at

Abstract

The impact of Si-segregates and varying deposition conditions on the structural and mechanical properties of oxidation-resistant Cr-Si-B_{2±z} coatings is studied from ambient, to elevated temperatures. Overstoichiometric, AlB₂-structured Cr-Si-B_{2±z} thin films with Si-content up to 15 at.% were synthesized on Ti-6Al-4V by magnetron-sputtering using a substrate bias of -120 V. The enhanced surface diffusion promotes mechanically superior, (001)-oriented coatings with hardness of $H \sim 30$ GPa up to a Si-content of 3 at.%. Higher Si-concentrations result in significant hardness loss to $H \sim 20$ GPa, related to a bias-independent solubility-limit in the CrB₂-structure and the formation of mechanically-weak Si grain-boundary segregates. The as-deposited hardness of all Cr-Si-B_{2±z} compositions is maintained after annealing to 800°C, despite the initiation of material recovery. A B/Cr-ratio-independent oxidation resistance up to 1400°C is demonstrated, underlining a minimum Si-content of 8 at.% to form a stable SiO₂-based scale. In line with the room-temperature hardness, increasing Si-contents are accompanied by decreasing fracture toughness, reducing from $K_{IC} \sim 2.9$ (Cr_{0.28}B_{0.72}) to ~ 1.7 MPa√m (Cr_{0.24}Si_{0.10}B_{0.66}). High-temperature cantilever bending up to 800°C revealed a brittle-to-ductile-like transition for Cr_{0.28}B_{0.72}, resulting in increased fracture toughness of $K_{IC} \sim 3.3$ MPa√m. Si-alloyed coatings show analogous behavior up to 400°C, whereas beyond, Si-segregates enable high-temperature plasticity and thus a significantly increased damage tolerance.

Keywords: Borides; PVD; Segregation; Oxidation resistance; High-temperature Micromechanics; Mechanical Properties;

1. Introduction

The mechanical properties of bulk materials at elevated temperatures cover a well investigated field of materials science [1–4]. This includes the temperature dependent description and analysis of physical properties including the modulus of elasticity, tensile strength, hardness, fatigue limits, and in particular the fracture resistance. Especially the latter property has been thoroughly described for a wide range of metals and alloys [5–10], technical ceramics [3,11–13], as well as intermetallics [14,15]. However, the high temperature fracture behavior of thin film materials – particularly ceramic coatings that are regularly applied in harsh environments to compensate for limiting bulk material properties – remain rather unexplored.

An emerging family of ceramic thin film materials that is targeted towards operating in ultra-high temperature applications due to their distinct refractory character, are transition metal diborides (TMB_2). This group of materials offers outstanding melting temperatures in excess of 3000 °C, paired with excellent thermal and chemical stability as well as high hardness and strength [16–20]. However, phase-pure TMB_2 suffer from comparably low oxidation resistance at temperatures beyond 600 °C, related to the formation of volatile B-O-(H)-based compounds when exposed to oxygen and water vapor containing environments [21,22]. This resulted in various alloying strategies to improve the oxidation behavior by means of solid solutions or multi-phased compounds. For bulk TMB_2 , the most promising improvements were achieved via the addition of Si-containing compounds (*e.g.*, SiC or $MoSi_2$), attributed to the formation of a stable, amorphous (boro)-silicate oxide scale [23–25].

Following this alloying strategy, recent studies highlighted the viability of using Si as a similarly potent oxide former in TM-Si-B₂-based coatings, revealing oxidation rates three orders of magnitude lower compared to TMB_2/SiC compounds at 1100 °C [26,27]. Especially Cr-Si-B₂-based coatings portrayed outstanding oxidation properties, exhibiting minimum mass gain and oxide scale growth rates even up to 1400 °C [28].

Inevitably, the addition of Si and corresponding compounds will alter the mechanical properties of TMB_2 binaries, both in terms of the alloying constituents as well as the temperature regime. Several works that would take advantage of SiC alloying for improved oxidation resistance in bulk ZrB_2 , simultaneously reported on enhanced specific strength and fracture resistance over a wide temperature range by tailoring the compositional arrangement [16,29–31]. In the case of ceramic thin films, a similar effectiveness of Si-alloying was observed for TiN. Despite only achieving limited improvements in oxidation resistance [32], a concomitant increase in hardness and fracture toughness of ~30 and ~60 % was observed, respectively [33]. Considering the complex bonding nature of AlB_2 -structured diborides, the limited research covering compositional and synthesis variations so far

suggests a negative impact of Si on the room temperature hardness for several TM-Si-B₂ [27]. Besides the known orientation dependency of the mechanical properties [34], this effect could be linked to Si grain boundary decorations formed during film growth upon exceeding a TMB₂ specific solubility limit [28]. In consequence, it seems imperative to investigate altered synthesis conditions, expanding the current viewpoint of the relationship between deposition parameters and the thermo-physical properties of TM-Si-B₂ thin films. Furthermore, with the improved oxidation behavior, increasing the knowledge on film hardness and fracture resistance at elevated temperatures appears a logical step forward.

While small-scale micromechanical testing at room temperature is crucial for the development of materials operated at ambient conditions, most applications of ceramic coatings necessitate testing at elevated temperatures. However, given the high complexity of low temperature measurements, possible difficulties are certainly amplified when introducing the influence of temperature. Thus, only few examples of high-temperature micromechanical testing on ceramic thin film materials exist to date. In an early work, Wheeler *et al.* [35] studied the temperature dependent compressive strength of CrN-based hard coatings by micro-pillar compression technique. In a series of experiments up to 500 °C, they highlighted that differences in the temperature dependent property evolution can cause a shift between rankings at room temperature and those at elevated temperatures. The results unequivocally demonstrated the necessity for high temperature property analysis. Furthermore, Best *et al.* [36] showed that thermal diffusion of Ga atoms in focused ion beam prepared micro-cantilevers affects the high temperature fracture toughness of CrN through intergranular embrittlement. An analogous micron sized geometry was used by Buchinger *et al.* [37], who studied the high temperature fracture behavior of TiN, both experimentally and theoretically. They revealed the negative impact of point defect annihilation at temperatures exceeding the deposition condition, leading to an irreversible decrease in fracture toughness throughout the entire temperature range. Finally, Drnovšek *et al.* [38] recently investigated the high temperature fracture properties of morphologically varying CrAlN (columnar) and CrAlSiN (nanocrystalline) by microcantilever bending technique. A similar behavior was revealed below the deposition temperature, while above a diverging fracture resistance was observed and attributed to the morphological differences.

In this work, we continue to explore the structural and mechanical properties of Si alloyed Cr-B_{2+z}-based thin films through targeted synthesis variations. The resulting compositional and structural ensemble is discussed in the context of room temperature nanoindentation and dynamic thermogravimetry up to 1400 °C. Thereby, novel insights on previously established Si solubility limits and optimum chemical compositions are described. Furthermore, vacuum annealing treatments are performed on coated Ti-6Al-4V, probing the temperature dependent hardness evolution as influenced

by thermally activated solid state processes. Finally, the high temperature fracture resistance of selected Cr-Si-B_{2±z} compositions is studied by detailed in-situ microcantilever bending experiments up to 800 °C.

2. Experimental

Direct current magnetron sputtering was used to grow AlB₂-type Cr-Si-B_{2±z} thin films from a 3-inch CrB₂ compound target (Plansee Composite Materials GmbH, 99.3% purity) operated in a lab-scale deposition system (in-house developed, base pressure below 1.0×10⁻⁶ mbar). Up to 16 Si platelets (3.5×3.5×0.38 mm³) were placed on the target racetrack to gradually adjusted the Si content in the synthesized coatings. The thin films were grown on (100)-oriented Si (20×7×0.38 mm³), single-crystalline, (1–102)-oriented Al₂O₃ (10×10×0.53 mm³), poly-crystalline Al₂O₃ (20×7×0.38 mm³) and mirror-polished Ti-6Al-4V (10×10×1 mm³) substrates. Following an ultrasonic pre-cleaning step in acetone and isopropyl, respectively, a heating sequence to a constant substrate temperature of $T = 550$ °C was performed. Prior to all depositions, Ar-ion etching was used to clean the substrate surface from native oxides and remaining residuals at a total pressure of $p = 50$ μbar and substrate bias potential of $U = -800$ V for 10 min. The substrates were fixtured in a rotating sample holder with a constant target-to-substrate distance of 90 mm. To additionally pre-clean the target surface and Si platelets for minimum oxygen contamination within the coatings, they were simultaneously sputter cleaned behind a shutter during the last 3 min of the Ar-ion etching sequence. The coatings were then synthesized at an Ar pressure of $p = 7$ μbar, a cathode current of $I = 0.4$ A ($\cong \sim 5$ W/cm²), and a substrate bias potential of $U = -120$ V. A consistent coating thickness of $t \sim 3$ μm was targeted, therefore the deposition time was adjusted accordingly.

The chemical composition of all Cr-Si-B_{2±z} thin films was evaluated using liquid inductively coupled plasma-optical emission spectroscopy (ICP-OES). For more details on the methodical procedure, see Ref. [27]. The crystal structure in the as-deposited as well as several annealed states was analyzed by X-ray diffraction, performed in Bragg-Brentano geometry on a PANalytical XPert Pro MPD equipped with a Cu-K_α radiation source (wave length $\lambda = 1.54$ Å, operated at 45 kV and 40 mA) and a strip detector (PANalytical X'Celerator). Furthermore, nanoindentation performed with an ultra-micro indentation system (UMIS) was used to determine the hardness and Young's modulus of all Cr-Si-B_{2±z} coatings. Stepwise increased indentation loads from 5 up to 22 mN (steps of 0.5 mN) were used to collect a minimum of 30 load-displacement curves for analysis according to the procedure proposed in Ref. [39]. Additional indents at forces up to 45 mN were added to probe for any substrate interference with the calculated results. For hardness evaluation an indentation depth smaller than 10 % of the entire coating thickness was maintained. Furthermore, the recorded Young's modulus data was fitted as

function of the indentation depth h_t using a power law relation and subsequently extrapolated to $h_t = 0$ for the coating-only modulus [40]. Finally, optical profilometry performed on a PS50 system (Nanovea) was employed to record the sample curvature of coated Si substrates. Combined with the modified Stoney-equation the residual stress state was determined [41,42].

The influence of Si alloying on the oxidation resistance of the Cr-Si-B_{2±z} coatings was studied by dynamic thermogravimetric analysis (TGA, Netzsch STA 449 F1, conducted in a Rhodium-type furnace). Therefore, polycrystalline Al₂O₃ substrates were weighed prior and after deposition to determine the coating-only mass, which serves as reference during the oxidation treatments performed up to 1400 °C (heating rate of 10 °C/min) in synthetic air (flow of 50 ml/min). The oxidation of the coating material was associated with the recorded mass change (detected at a resolution of 0.1 µg). Reference measurements on uncoated Al₂O₃ substrates showed that the material is inert in the investigated temperature regime, hence a contribution from the substrate to the recorded mass change can be excluded [27].

All Cr-Si-B_{2±z} coatings deposited onto Ti-6Al-4V were vacuum annealed in a Centorr LF22-2000 vacuum furnace at temperatures of $T = 400, 600, \text{ and } 800$ °C for 30 min (heating rate of 20 K/min, passive cooling at >50 K/min to 200 °C). A base pressure below 1.0×10^{-5} mbar was established before each annealing treatment. Afterwards, all samples were again analyzed by X-ray diffraction and nanoindentation.

Selected Cr-Si-B_{2±z} thin films (on Ti-6Al-4V) were investigated concerning their high-temperature fracture toughness using microcantilever bending experiments [43]. These tests were performed on a FemtoTools FT-NMT04 *in situ* nanoindentation system equipped with a sample heater stage and a diamond wedge tip (contact length of 10 µm). The experiments were conducted at room temperature (RT) as well as at $T = 400, 600, \text{ and } 800$ °C, with additional tests performed in the annealed state after cooling down to room temperature (RT p.a.). Therefore, free standing micro-cantilever specimen were prepared by focused ion beam milling (FIB) using Ga⁺-ions in a FEI Scios 2 DBFIB microscope and in accordance with the guidelines suggested in Ref. [44]. Based on a mirror polished cross-section of a coated Ti-6Al-4V substrate, the micro-cantilevers were prepared by the following milling sequence: (i) Rough milling of the cantilever outlines through the coating material and ~10 µm deep into the substrate (ion beam aligned perpendicular to the coated surface, ion beam current of 30 nA). This initial cantilever geometry is aligned parallel to and placed 2 µm from the front edge. (ii) Removing of the substrate material beneath the rough-cut cantilever and fine milling to the final thickness, producing a coating-only beam (ion beam aligned perpendicular, ion beam current reduced stepwise from 30 to 1 nA). (iii) Fine milling of the cantilever contour to the final dimensions and fabrication of a pre-notch (ion beam aligned perpendicular to coated surface, ion beam current reduced stepwise from 5 to 1 nA, pre-notch produced at a milling current of 50 pA). The cantilevers were produced to a final

geometry of length (l) \times width (b) \times height (w) = $t \times t \times 6t \mu\text{m}^3$, whereby t denotes the coating thickness, with a pre-notch depth of $a_0 \sim 400\text{-}450$ nm. Thin material sections were left intact on both sides of the pre-notch, serving as initiation sites for a sharp crack. Temperature calibration between the tip and sample was conducted using the balancing function provided in the operating software. The procedure performs shallow indentations every few seconds in the bulk coating area close to the cantilever specimen, wherein the force response on the tip upon unloading is recorded. The tip current is adjusted accordingly until a sufficiently low thermal discrepancy (*i.e.*, force response) is achieved. Details on the procedure are listed in Ref. [45]. The bending experiments were performed in displacement-controlled mode at a deflection rate of $10 \text{ nm} \cdot \text{s}^{-1}$.

Based on measurements of the individual fractured cantilever cross-section in combination with the recorded maximum force at failure, a value for the critical stress intensity K_{IC} of each cantilever was calculated utilizing the formalism outlined in [46]:

$$K_{IC} = \frac{F_C l}{bw^2} \times f\left(\frac{a_0}{w}\right)$$

with

$$f\left(\frac{a_0}{w}\right) = 1.46 + 24.36\left(\frac{a_0}{w}\right) - 47.21\left(\frac{a_0}{w}\right)^2 + 75.18\left(\frac{a_0}{w}\right)^3$$

At least 4 samples were tested and evaluated at every temperature step.

3. Results & Discussion

3.1. Chemical composition

Figure 1 presents the chemical compositions of all Cr-Si-B_{2±z} thin films in the context of a ternary phase diagram. The depicted compositional range is extended with guidelines (corresponding to narrow two-phase fields) connecting stoichiometric CrB₂ with Si and CrSi₂, to indicate possible phase mixtures in the as deposited state. Chemical analysis using ICP-OES revealed a linear increase in the Si alloying content within the Cr-Si-B_{2±z} thin films, showing an almost 1:1 correlation between the number of Si platelets placed on the target racetrack during sputtering and the resulting atomic concentration. Hence, utilizing 2, 4, 6, 8, 12, and 16 Si platelets for the synthesis process resulted in corresponding Si compositions of 2, 3, 4, 6, 10, and 15 at.%, respectively. Furthermore, the data reveals a clear shift of all chemistries towards B-rich compositions – *i.e.*, a deviation from the stoichiometric CrB₂ + Si line – suggesting a B-overstoichiometry especially for lower alloyed thin films. Starting with a B concentration of 72 at.% in the unalloyed coating, an overall decrease is observed from 72 at.% for Cr_{0.26}Si_{0.02}B_{0.72}, down to 62 at.% in Cr_{0.23}Si_{0.15}B_{0.62} with increasing Si fraction. Regarding the B:Cr ratios,

the impression of excess B content is underlined by values increasing from 2.6 up to 2.8 for the highest Si containing coating. Nevertheless, the chemical compositions reveal an actually replacement of both B and Cr in the stoichiometric 2:1 ratio, respectively.

It is imperative to mention that the overstoichiometry is inherently dependent on the actual lattice occupation of the Si atoms as well as the individual contribution of the constitutional elements to the phase formation. As previously revealed by detailed DFT calculations, the Cr-Si-B₂ system prefers the incorporation of substitutional Si atoms on the Cr- and B-lattice for lower alloying fractions, whereas for higher concentrations only Cr replacement yields chemically stable configurations [28]. Moreover, a theoretically proposed Si solubility limit close to 8 at.% in the AlB₂-structure, which was experimentally determined with a lower value of ~3-4 at.%, suggests that all coatings with an alloying fraction higher than Cr_{0.26}Si_{0.03}B_{0.71} obtain Si grain boundary segregations in the as-deposited state. Thus, the presence of a B overstoichiometry in all thin films, with possible contributions of B to the Si grain boundary decorations – in agreement with the respective chemical composition within the phase fields in Figure 1 – can be expected.

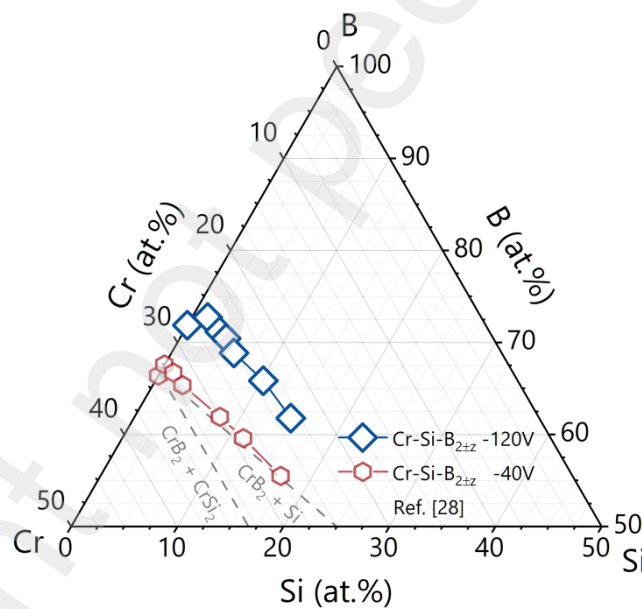


Figure 1: Ternary phase diagram depicting the chemical composition of all synthesized Cr-Si-B_{2+z} coatings (blue diamonds). The chemistry of corresponding thin films deposited at a substrate bias voltage of $U = -40$ V (red hexagons, Ref. [28]) as well as guidelines for two-phase fields are included. The axis scaling is reduced for improved visibility of the individual data points.

The observed increase in B over the prototypical Cr_{0.33}B_{0.67} target composition is seen in the prevalent synthesis conditions, especially in the film growth conditions on the substrate surface created by the high bias potential of $U = -120$ V. When compared to data of previous Cr-Si-B_{2+z} thin films deposited at a bias potential of $U = -40$ V, (see Figure 1, red hexagons, other deposition conditions were analogous), a noticeable impact of the substrate bias to promote higher B contents in the growing thin films is

evident. Furthermore, the comparison reveals a very alike behavior in terms of the B- and Cr-replacement with increasing Si alloying fraction, although overall higher Si contents could be reached at a lower substrate bias. Interestingly, the increase in B content with enhanced bias potential appears counterintuitive, since lighter elements typically suffer from increased scattering and resputtering effects during the synthesis process. However, the close matching atomic weight between Ar⁺ ions and Cr film atoms yields a more effective energy transfer and lifts the preferred resputtering tendency from the B atoms, which causes the recorded overstoichiometry. A similar effect was previously observed during the sputter deposition of TiB₂ using similar bias voltage variations [47].

3.2. Phase formation

Apart from the impact on thin film chemistry, the chosen synthesis conditions will also be reflected in the phase formation of the Cr-Si-B_{2±z} coatings. Figure 2 presents the recorded X-ray diffractographs, arranged with increasing Si content from bottom to top. In addition, the right panel includes the (001)-texture coefficient for every diffractograph according to the following equation:

$$TC_{(hkl)} = \frac{I_{(hkl)}/I_{0(hkl)}}{\frac{1}{N} \sum_N I_{(hkl)}/I_{0(hkl)}}$$

where $I_{(hkl)}$ is the diffracted intensity on the (hkl) -lattice plane, $I_{0(hkl)}$ is the corresponding reference intensity for powdered CrB₂ [48], and N equals 3, representing the (001), (100), and (101) planes. The diffraction studies demonstrate that all Cr-Si-B_{2±z} coatings adopt the AlB₂-type hexagonal structure, irrespective of the alloying content and the B overstoichiometry. The distinct impact on phase formation created through the high bias voltage within all depositions is nicely demonstrated when comparing the unalloyed Cr_{0.28}B_{0.72} coating to a Cr_{0.34}B_{0.66} composition, grown at a lower substrate bias of -40 V (see Figure 2, bottom). Apparently, increasing the surface mobility for arriving film constituents through increased Ar⁺ bombardment results in a shift from (101)-, towards film growth conditions preferring the (001)-direction. Concomitantly, with a denser microstructure – as evidenced by scanning electron microscopy of Si fracture cross-sections (see Supplementary) – TMB₂ thin films show a desirable optimum in film hardness in the (001)-direction [34] (detailed discussion follows in Section 3.3). Up to a Si content of 3 at.% in Cr_{0.26}Si_{0.03}B_{0.71}, film growth conditions remain unaltered in the preferred (001)-orientation, although an increasing contribution from differently oriented grains is noticeable. Further increasing the alloying content results in a shift towards the (100)-direction for both Cr_{0.25}Si_{0.04}B_{0.71} and Cr_{0.25}Si_{0.06}B_{0.69}, before diverting back to (001)-oriented for the Cr_{0.24}Si_{0.10}B_{0.66} composition (see Figure 2, right panel). Finally, the diffractograph for the highest Si containing coating Cr_{0.23}Si_{0.15}B_{0.62} suggests equally oriented grains and a clear reduction of the diffracted intensities, pointing towards a decreasing average grain size. This contrasts with previous findings for Cr-Si-B_{2±z}

deposited at a bias voltage of -40 V, where a similar grain refinement was already present for lower alloying fractions, starting at Si concentrations of ~4 at.% [28]. This effect could be correlated with surpassing the Si solubility limit in the hexagonal CrB_2 structure, leading to the energetically favored segregation of the alloying species to grain boundary sites. Although an extension of this solubility limit with increased bias voltage is unlikely, the growth of larger crystalline domains is enabled up to 10 at.%, following the enhanced adatom mobility. Finally, in view of the phase fields included in Figure 1, no additional crystalline structure was detected by X-ray diffraction technique throughout all experimentally studied $\text{Cr-Si-B}_{2\pm z}$ compositions.

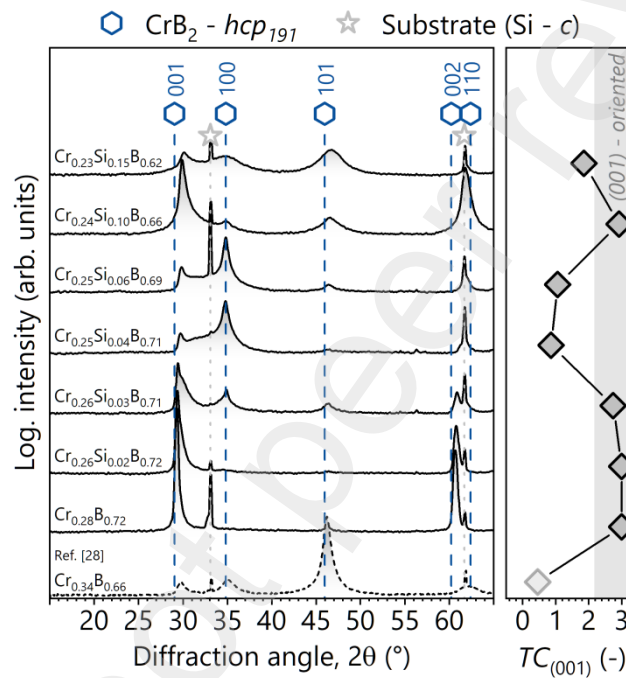


Figure 2: X-ray diffractograms of $\text{Cr-Si-B}_{2\pm z}$ thin films deposited on Si substrate with increasing alloying content from bottom to top. A diffractogram recorded from a $\text{Cr}_{0.34}\text{B}_{0.66}$ coating deposited with a substrate bias of $U = -40$ V is included for comparison on the bottom (taken from Ref. [28]). In addition, standardized reference pattern for hexagonal CrB_2 (space group 191, blue hexagons, [48]) and cubic Si (substrate, grey stars, [49]) are added for structural comparison. The intensity ratio of the (001)-peak is further presented in the right panel, with data points matching the diffractograms in y-direction.

3.3. Mechanical properties at room temperature

The mechanical properties of the $\text{Cr-Si-B}_{2\pm z}$ thin films are summarized in Figure 3, presenting the residual biaxial stress state as well as the hardness and Young's modulus versus the Si alloying content. While nanoindentation experiments were obtained from thin films on Ti-6Al-4V, residual stress measurements could solely be obtained from coated Si substrate through curvature measurements. The high degree of (001)-orientation within several $\text{Cr-Si-B}_{2\pm z}$ samples prohibits a consistent stress analysis on the Ti-substrate using the $\sin^2(\psi)$ -approach. Considering the impact of varying thermal

expansion coefficients between the coatings ($\alpha_a^{CrB_2} = 10.8 \times 10^{-6}K^{-1}$, $\alpha_c^{CrB_2} = 6.3 \times 10^{-6}K^{-1}$, [50]) and both substrate materials ($\alpha^{Si} = 2.5 - 4 \times 10^{-6}K^{-1}$ [51], $\alpha^{Ti-6Al-4V} = 8 - 10 \times 10^{-6}K^{-1}$ [52]), a shift towards a more compressed stress state can be assumed for all coatings on the Ti-alloy (note, the absolute value may still be located in the tensile regime). Furthermore, depending on a possible template effect, the different substrate materials may entail altered film growth conditions and thus growth-related stresses. However, comparison of X-ray diffractographs obtained from depositions on both substrates (compare Figures 2 and 6) revealed identical crystallographic distributions as well as diffracted intensities throughout the Cr-Si-B_{2±z} compositions. In addition, the influence of altered synthesis conditions is addressed by a complementary data set taken from Ref. [28] for a Cr_{0.34}B_{0.66} coating, deposited with bias voltage of $U = -40$ V (see also Figure 2, bottom).

Measurements on the unalloyed Cr_{0.28}B_{0.72} coating reveal a slight compressive stress state at $\sigma \sim -0.25$ GPa combined with an excellent hardness of $H = 29.1 \pm 1.1$ GPa and a Young's modulus of $E = 339 \pm 7$ GPa. When compared to the Si-free reference coating [28], a striking difference of over 5.5 GPa in film hardness is noticed, while the Young's modulus increased by approximately 45 GPa. This improvement is rationalized by the difference in preferred growth orientation and an overall densification of the film microstructure due to the increased bias potential. The results unequivocally highlight the distinct anisotropy of this AlB₂-structured diboride, pointing out highest film hardness in the (001)-orientation [34]. Moreover, the densified film structure is further correlated with the observed increase of the Young's modulus, which is likely the result of enhanced cohesive strength on grain boundary sites.

Introducing Si to the Cr-B_{2±z} thin films results in a shift of the residual stress state towards the tensile regime, with the highest value recorded for the Cr_{0.25}Si_{0.04}B_{0.71} composition at $\sigma \sim 0.8$ GPa. This trend appears to be decoupled from the film orientation, since all coatings between 4 and 6 at.% Si maintain a similar stress profile despite exhibiting an increasing (100)-orientation. A possible explanation is seen in reduced compressive growth stresses resulting from the increasing Si alloying content. A comparable evolution is observed for the Young's modulus, revealing a concomitant increase up to $E = 383$ GPa for Cr_{0.25}Si_{0.04}B_{0.71}. In agreement with previous reports on the elastic constants of CrB₂ ($E_{(100)}^{CrB_2} = 531$ GPa, $E_{(001)}^{CrB_2} = 302$ GPa), the enhanced contribution of the stiffer (100)-orientation is attributed to cause an increase in the elastic modulus. The hardness data shows a significant decrease for Si concentrations above 4 at.%, with values drastically falling from $H = 29.7 \pm 1.0$ GPa for Cr_{0.26}Si_{0.03}B_{0.71} down to 22.5 ± 0.9 GPa for Cr_{0.25}Si_{0.04}B_{0.71}. These results reflect the divergence from the (001)-orientation with increasing Si content and the initial segregation of the alloying species towards grain boundary sites during the film growth process. Consequently, this also underpins the previous correlation to a solubility limit located the same alloying regime (see Section 3.2).

The coatings with the highest Si content, Cr_{0.24}Si_{0.10}B_{0.66} and Cr_{0.23}Si_{0.15}B_{0.62}, exhibit rather low residual

stress values at $\sigma \sim 0.1$ and -0.2 GPa, respectively. In addition, the increasing segregation of Si to the grain boundaries (see Section 3.1 and Ref. [28]) leads to a refined microstructure and an overall increase in weaker-connected grain boundary volume, resulting in a decrease of the Young's modulus to $E = 296 \pm 4$ GPa. Moreover, the film hardness assumes rather constant values at $H \sim 20$ GPa for all Cr-Si-B_{2±z} compositions above 6 at.% Si, also reflecting the dominating aspect of the weaker connection on grain boundary sites. Nevertheless, the results highlight that utilizing energetic ion bombardment for the deposition of Cr-Si-B_{2±z} thin films lead to an increase in film hardness between 4 and 6 GPa over compositionally similar coatings deposited at $U = -40$ V.

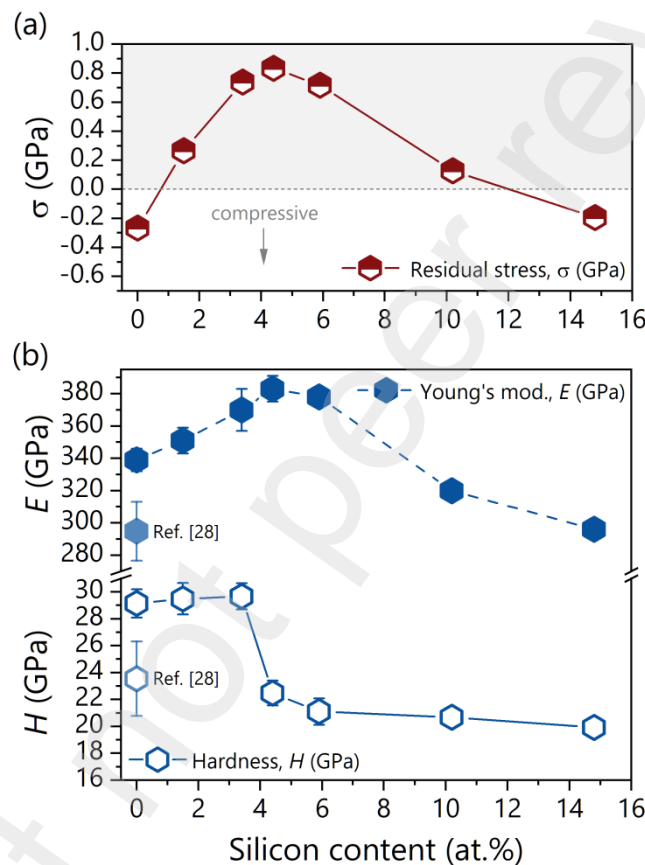


Figure 3: (a) Residual stress of the synthesized Cr-Si-B_{2±z} thin films on Si substrate as function of the Si alloying content. (b) Hardness and Young's modulus data for the corresponding compositions in (a) collected on Ti-6Al-4V substrate. For comparison, (a) and (b) contain data for a Cr_{0.34}B_{0.66} coating deposited with a substrate bias of $U = -40$ V taken from Ref. [28] (see Figure 2, bottom).

3.4. Thermogravimetric analysis

Previous dynamic oxidation experiments of various Si alloyed TM-B_{2±z}-based thin films highlighted the capabilities of this alloying route to significantly improve the oxidation resistance over the binary materials [27]. Next to the effective Si alloying content, the ratio between the boron and transition metal was demonstrated to crucially impact the oxidation behavior of these materials. Especially boron

deficient TM-B_{2-z} compositions revealed improved oxidation protection related to the absence of B-rich grain boundary decorations, which are usually responsible for providing fast-track oxidation pathways [53,54]. Therefore, dynamic thermogravimetric experiments were performed on the synthesized Cr-Si-B_{2±z} thin films to investigate the oxidation behavior of drastically increased B/TM-ratios and prove the robustness of the Si alloying route (see Figure 4).

In relation to analogous experiments performed on Cr-Si-B_{2±z} coatings obtaining a B/TM ratio of ~2.0 [28] and ~2.2 [27], the oxidation tests resulted in an identical protective performance, shifting the onset of oxidative mass gain consistently from $T = 600$ up to 1100 °C, depending on a “sufficient” Si alloying content. Even for “insufficiently” alloyed compositions, a very similar oxidation response was reported, resulting in a stepwise formation of mixed B₂O₃ and Cr₂O₃ scales. The mass change data during oxidation up to 1400 °C presented in Figure 4 highlights, that even compositions with a B/TM-ratio approaching 2.8 (see also Figure 1) obtain an entirely unchanged, excellent oxidation resistance throughout the corresponding Si compositions. While, the coatings synthesized with a Si content ≤ 4 at.% undergo progressive oxidation starting at $T = 600$ °C, both coatings with an alloying content ≥ 10 at.% depict a fully stable mass signal up to $T = 1200$ °C. Consequently, the results strongly suggest that the mechanism responsible for the oxidation protection – identified as the thermally activated precipitation of Si on the coating surface [28] – is decoupled from the chemical composition of the CrB_{2±z} host structure. In other words, the oxidation resistance scales solely with the effective Si concentration. Nevertheless, a possible contribution of excess boron to the high temperature performance is assumed in the shift of the oxidation onset temperature from previous experiments, which is increased by ~ 100 °C to $T = 1200$ °C within the highly overstoichiometric Cr-Si-B_{2±z} coatings. A possible explanation could be seen in enhanced Si diffusion along the increased grain boundary volume, decorated with both amorphous B- and Si-rich phases.

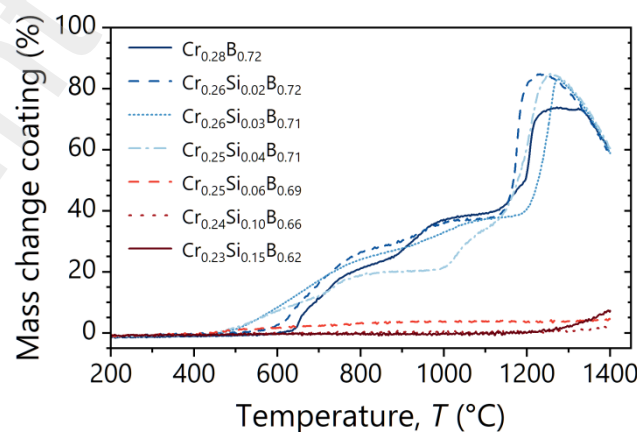


Figure 4: Thermogravimetric analysis of Cr-Si-B_{2±z} thin films on polycrystalline Al₂O₃ substrate up to $T = 1400$ °C (10 K/min heating rate) in synthetic air environment. The mass change of the coating material is presented as function of the annealing temperature and indicates the onset of sample oxidation. Note, pretests confirmed the inert behavior of the substrate

material in the analyzed temperature range.

Regarding the transition from “insufficiently” to “sufficiently” alloyed compositions, the mass signal recorded for the $\text{Cr}_{0.25}\text{Si}_{0.06}\text{B}_{0.69}$ coating points towards a threshold concentration. Despite the premature onset of oxidation close to $T = 600$ °C, the coating is able to form a stable SiO_2 -based scale that remains intact up to $T = 1400$ °C. This result is in excellent agreement with a previously determined minimum Si content of 8 at.% to achieve negligible mass gain up to $T = 1100$ °C [28].

3.5. Hardness & structural evolution up to 800 °C

Vacuum annealing treatments were performed on all Cr-Si-B_{2±z} thin films for 30 min at temperatures of $T = 400, 600,$ and 800 °C. The annealed samples were subsequently investigated by nanoindentation and X-ray diffraction technique to reveal the film hardness in the annealed state as well as the phase stability and diffusion driven interaction with the Ti-6Al-4V substrate. Figure 5 presents the recorded hardness as function of the annealing temperature. Based on the distribution measured in the as-deposited state (see Figure 3), the data reveals an almost unaffected film hardness throughout the temperature range for all compositions with Si content ≤ 6 at.%. This is especially interesting, considering the Cr-Si-B_{2±z} compounds are known to experience thermally induced segregation of the alloying species at $T > 600$ °C, followed by initial recovery/recrystallisation of the remaining solid solution as well as separation into the binary diboride and pure Si [28]. These solid-state reactions are nicely visible in the X-ray diffractographs presented in Figure 6, recorded in the post-annealed state on the binary $\text{Cr}_{0.28}\text{B}_{0.72}$ (lower section) and $\text{Cr}_{0.25}\text{Si}_{0.06}\text{B}_{0.69}$ coating (middle section). Thermal treatment of the Si-free coating results in minor structural changes throughout all annealing temperatures. Starting at $T = 600$ °C, slight sharpening of the (001)-peak is noticeable, related to initial recovery of point defects (note the deposition temperature of $T = 550$ °C). Moreover, at $T = 800$ °C additional peaks identified as the orthorhombic monoborides of Cr and Ti, occur. The latter two structures suggest an interdiffusion between (excess) boron from the coating and the Ti-alloy substrate. Given the low intensities recorded for the mono-borides, it is assumed that both structures are confined to the interface near region without affecting the surface hardness of the coating. The higher Si containing $\text{Cr}_{0.25}\text{Si}_{0.06}\text{B}_{0.69}$ sample shows a similar behavior, with a more pronounced recovery/recrystallisation of the CrB_2 -structure starting above $T = 600$ °C. Next to the diffraction spots indicating the previously observed mono-borides, the coating also exhibits the precipitation of Si next to the formation of a hexagonal CrSi_2 phase at $T = 600$ °C. Comparison to previous oxidation experiments performed on a $\text{Cr}_{0.29}\text{Si}_{0.11}\text{B}_{0.60}$ coated Al_2O_3 substrate [28] reveals that the disilicide formation is independent of the substrate material and annealing environment, hence a distribution around Si precipitates is expected. Still, the structural changes within both coatings appear to be in an initial stage at $T = 800$ °C, where

the presence of additional phases is balanced by the unaffected coating material – also in terms of the stress state – resulting in a maintained film hardness.

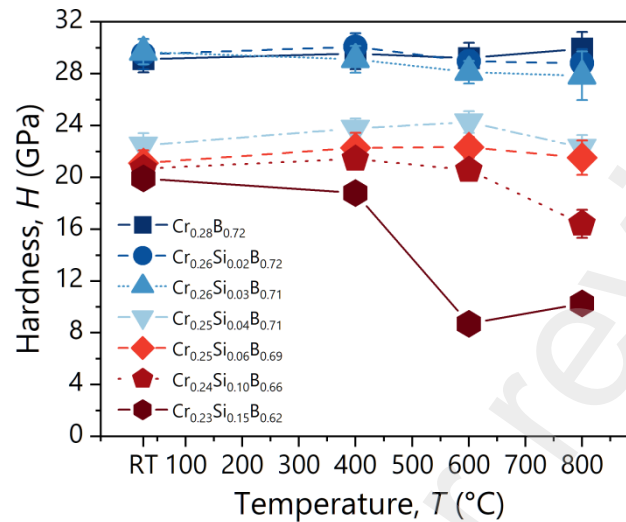


Figure 5: Hardness values of Cr-Si-B_{2±2} thin films on Ti-6Al-4V substrate at room temperature and after vacuum annealing at $T = 400, 600,$ and $800\text{ }^{\circ}\text{C}$ (holding duration of 30 min).

Increasing the Si content beyond 10 at.% permits a maintained coating hardness up to $T = 600\text{ }^{\circ}\text{C}$ for the $\text{Cr}_{0.24}\text{Si}_{0.10}\text{B}_{0.66}$, whereas the $\text{Cr}_{0.23}\text{Si}_{0.15}\text{B}_{0.62}$ coating already reveals a decreasing trend. At $T = 800\text{ }^{\circ}\text{C}$, both compositions show an effective reduction in hardness from $H = 20.7 \pm 0.5$ and 19.9 ± 0.4 GPa down to $H = 16.4 \pm 1.1$ and 10.3 ± 0.5 GPa, respectively. Comparing the structural evolution recorded for the $\text{Cr}_{0.23}\text{Si}_{0.15}\text{B}_{0.62}$ coating in Figure 6 (top section) to lower Si containing compositions (see Figure 6, middle section) reveals a similar trend. However, both the recovery/recrystallisation of the Cr-Si-B₂ solid solution as well as the segregation of Si are more pronounced at $T = 600\text{ }^{\circ}\text{C}$, resulting in increased peak intensities for both structures at $T = 800\text{ }^{\circ}\text{C}$. This suggests, that the driving force of these solid-state reactions actually scales with the initial Si content in the thin films. An increased diffraction intensity is further observed for the CrSi_2 phase, associated with the overall higher Si reservoir available in the coating.

Related to the protective mechanism responsible for the increased oxidation resistance, as confirmed by TG analysis in Figure 4, both coatings form a continuous Si surface layer starting at $T = 600$ or $800\text{ }^{\circ}\text{C}$, depending on the respective Si concentration. Consequently, the recorded loss in hardness for both compositions is attributed to the increasing contribution of this softer surface layer to the nanoindentation experiments. In fact, comparison with literature reports yields a perfect agreement between the hardness of the $\text{Cr}_{0.23}\text{Si}_{0.15}\text{B}_{0.62}$ coating annealed at $T = 600$ and $800\text{ }^{\circ}\text{C}$ with values

recorded for pure Si [55].

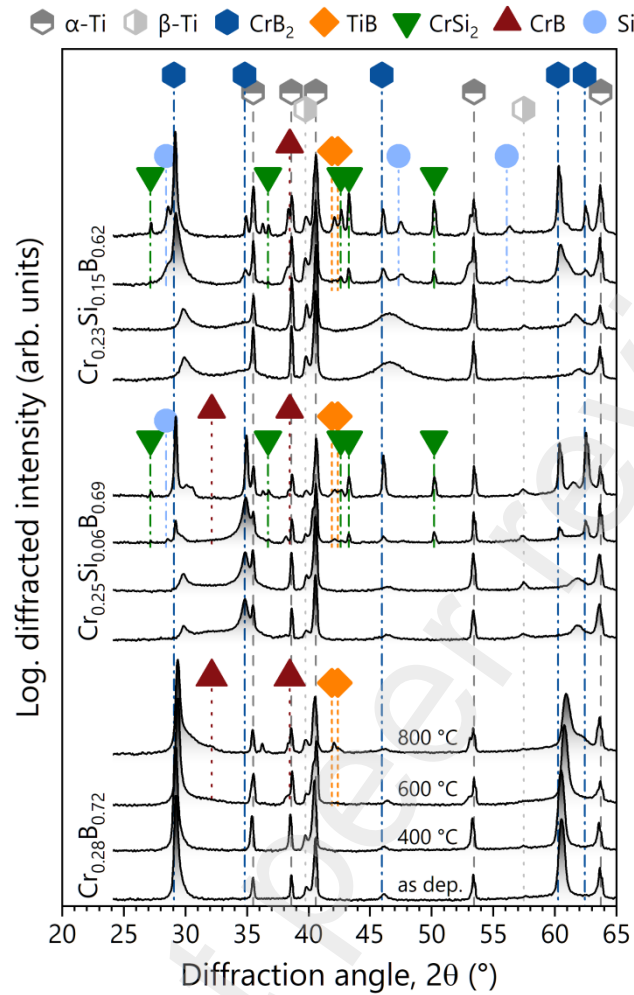


Figure 6: X-ray diffractograms of three selected Cr-Si-B_{2+z} compositions on Ti-6Al-4V are presented in the as-deposited state as well as after vacuum annealing at 400, 600, and 800 °C for 30 min. The diffractograms are arranged in three sections with increasing Si content from bottom to top (Cr_{0.28}B_{0.72}, Cr_{0.25}Si_{0.06}B_{0.69}, Cr_{0.23}Si_{0.15}B_{0.62}). Within each section, the data is sorted with increasing annealing temperature from bottom to top. Standardized reference pattern for hexagonal CrB₂ (space group 191, blue hexagons, [48]), cubic Si (light blue circle, [49]), hexagonal CrSi₂ (green triangle, [56]), orthorhombic CrB (red pyramid, [57]) and TiB (orange diamond, [58]), as well as for the dual-phased Ti-6Al-4V substrate material (grey hexagons, α-Ti [59], β-Ti [60]) are included.

3.6. In-situ high-temperature fracture toughness

The fracture properties at elevated temperatures were studied for selected Cr-Si-B_{2+z} coatings by in-situ high-temperature cantilever bending experiments up to $T = 800$ °C. Figure 7 presents the recorded load-displacement data normalized in terms of the stress intensity and bending strain for all compositions within the studied temperature range. In addition, Figure 8 summarizes the calculated critical stress intensity (*i.e.*, the fracture toughness) as function of the annealing temperature.

The bending tests performed on the unalloyed $\text{Cr}_{0.28}\text{B}_{0.72}$ resulted in a perfectly linear-elastic material response over the entire loading sequence throughout all temperature steps up to $T = 800\text{ }^\circ\text{C}$ (see Figure 7a). The initial fracture toughness in the as-deposited state was calculated with $K_{IC} = 2.87 \pm 0.05$ MPa $\sqrt{\text{m}}$ (see Figure 8). This value is considerably lower when compared to a previous work reporting on a fracture toughness of $K_{IC} = 4.3 \pm 0.3$ MPa $\sqrt{\text{m}}$ for an almost stoichiometric $\text{Cr}_{0.35}\text{B}_{0.65}$ coating [61]. Apart from the unambiguous influence of varying synthesis conditions, Fuger *et al.* [62] recently highlighted the negative impact of boron enriched grain boundaries – as also assumed within the overstoichiometric $\text{Cr}_{0.28}\text{B}_{0.72}$ – on the fracture toughness of TiB_{2+z} thin films.

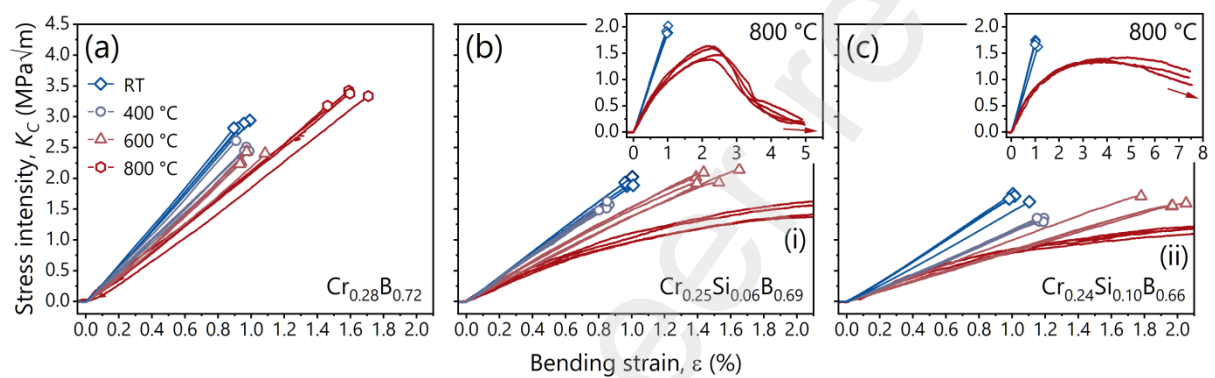


Figure 7: Normalized stress intensity - bending strain curves recorded during in-situ micro-cantilever bending experiments performed at room temperature as well as $T = 400, 600,$ and $800\text{ }^\circ\text{C}$ for (a) $\text{Cr}_{0.28}\text{B}_{0.72}$, (b) $\text{Cr}_{0.25}\text{Si}_{0.06}\text{B}_{0.69}$, and (c) $\text{Cr}_{0.24}\text{Si}_{0.10}\text{B}_{0.66}$. All thin films were deposited on Ti-6Al-4V substrate. The inserts in (b) and (c) depict a comparison of the data recorded at RT and $800\text{ }^\circ\text{C}$ over an extended strain range.

Similar to the observations in Ref. [38], increasing the sample temperature from RT to $T = 400$ and $600\text{ }^\circ\text{C}$ is followed by a linear decrease of the fracture toughness to $K_{IC} = 2.5 \pm 0.07$ and 2.34 ± 0.09 MPa $\sqrt{\text{m}}$, respectively (see Figure 8). Due to the absence of clear microstructural changes from recovery or recrystallisation in the corresponding temperature regime (compare with Figure 6), a connection is drawn to temperature enhanced lattice vibrations and a concomitant decrease of the interatomic bond strength. This explanation is in line with measurements on the thermo-physical properties of several TMB_2 , revealing a monotonic decrease of the elastic constants in the temperature range up to $T = 1100\text{ }^\circ\text{C}$ [63]. Regarding the maximum strain at failure for these samples, all bending experiments up to $T = 600\text{ }^\circ\text{C}$ resulted in consistent value of $\epsilon \sim 0.9\%$ (see Figure 7a).

Upon increasing the temperature to $T = 800\text{ }^\circ\text{C}$ during the bending experiments, a significant increase in the fracture resistance to $K_{IC} = 3.33 \pm 0.09$ MPa $\sqrt{\text{m}}$ as well as in the strain-to-failure at $\epsilon \sim 1.6\%$ is recorded. Similar trends in the high-temperature fracture toughness can be observed for various fine-

grained technical ceramics (*e.g.*, alumina or yttria stabilized zirconia) beyond a brittle-to-ductile transition temperature. Within these materials, thermal activation of grain boundary sliding enables large scale plastic deformation [64,65]. Although the stress - strain response of the $\text{Cr}_{0.28}\text{B}_{0.72}$ sample does not reveal any plastic deformation in the sense of a brittle-to-ductile transitions at $T = 800\text{ }^\circ\text{C}$ (see Figure 7a), an increased contribution from fracture energy dissipating mechanisms is unequivocally demonstrated. To the authors best knowledge, no thermally activated strengthening of atomic bonds on the boron decorated grain boundaries is applicable. Therefore, a temperature dependent mechanism allowing for enhanced movement between adjacent grains through sliding along these amorphous defect sites, is proposed. In line with the structural analysis in Figure 6, this assumes that no significant microstructural change – *i.e.*, a complete recrystallisation or reordering of the original grain boundaries – occurs at $T = 800\text{ }^\circ\text{C}$ within the material. This is underlined by complementary measurements conducted at room temperature after sample cooling, resulting in a fracture toughness of $K_{IC} = 2.91 \pm 0.12\text{ MPa}\sqrt{\text{m}}$, which is well within the accuracy of the fracture resistance recorded in the as-deposited state (see Figure 8). Furthermore, SEM images taken of the cantilever cross-sections for data analysis show no significant change in the apparent fracture morphology throughout all temperature steps (see Figure 9, upper row $\text{Cr}_{0.28}\text{B}_{0.72}$). The images consistently suggest a preferred fracture along the column boundaries.

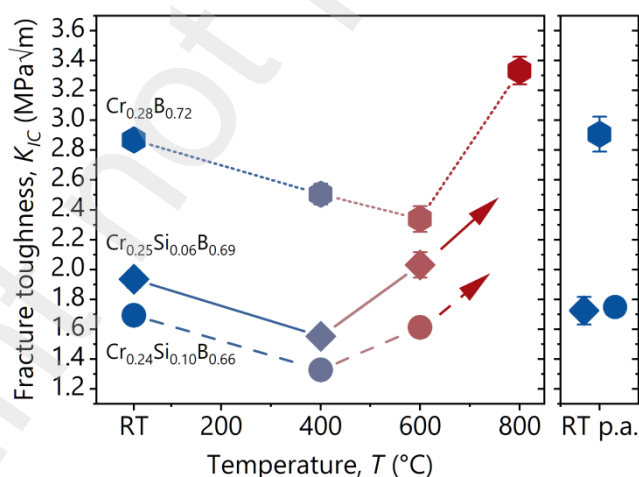


Figure 8: Calculated fracture toughness at room temperature (RT) as well as $T = 400, 600,$ and $800\text{ }^\circ\text{C}$ for $\text{Cr}_{0.28}\text{B}_{0.72}$ (hexagons), $\text{Cr}_{0.25}\text{Si}_{0.06}\text{B}_{0.69}$ (diamonds), and $\text{Cr}_{0.24}\text{Si}_{0.10}\text{B}_{0.66}$ (circles). The corresponding fracture toughness measured at room temperature after sample cooling (RT p.a.) is included in the right panel (the lower two data points are horizontally offset for better visibility).

As recently pointed out by Buchinger *et al.* [37], the recovery of the as-deposited fracture toughness strongly depends on the annihilation of point defects at elevated temperatures. However, the study focuses on a highly crystalline TiN coating for their high temperature experiments, which clearly lacks the influence of fracture dominating grain boundary phases when compared to the $\text{Cr}_{0.28}\text{B}_{0.72}$ coating. This demonstrates, why a fracture toughness matching the as-deposited value could be regained for the diboride thin film, whereas the nitride coating suffered a noticeable decrease in the annealed state. Nevertheless, the proposed high temperature behavior of the binary diborides needs further clarification, thus will be thoroughly reviewed in a follow-up study using a series of over- and understoichiometric TMB_2 thin films.

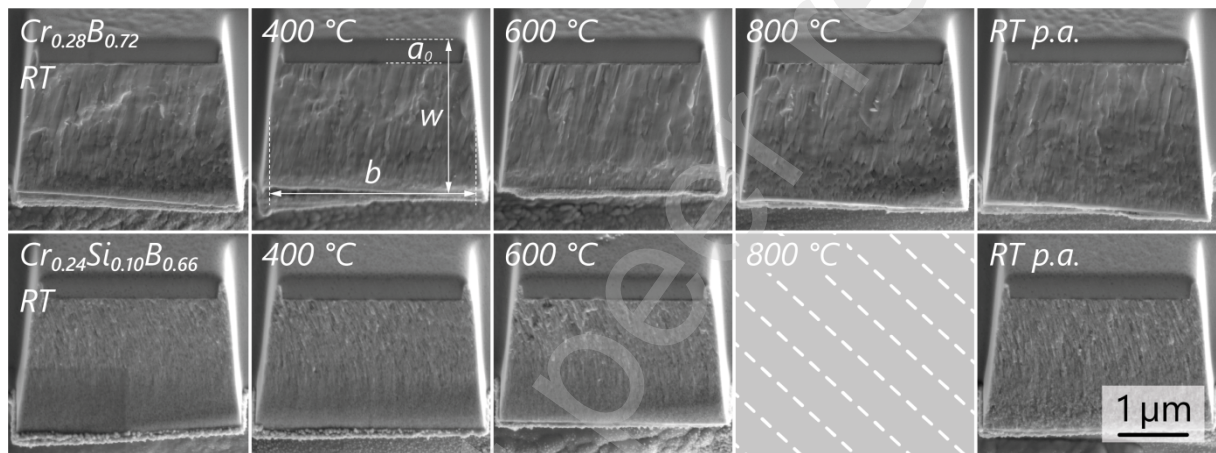


Figure 9: Representative SEM images of the fractured cantilever cross-sections for all temperature steps on both, $\text{Cr}_{0.28}\text{B}_{0.72}$ (upper row) and $\text{Cr}_{0.24}\text{Si}_{0.10}\text{B}_{0.66}$ (lower row). The images were recorded after the final experiment at RT, hence all cross-sections exposed during prior tests experienced annealing up to 800 °C. The fracture cross-section for $\text{Cr}_{0.24}\text{Si}_{0.10}\text{B}_{0.66}$ at 800 °C could not be recorded, since the cantilever was still attached to the base after the bending experiment.

Room temperature bending experiments on both the $\text{Cr}_{0.25}\text{Si}_{0.06}\text{B}_{0.69}$ and $\text{Cr}_{0.24}\text{Si}_{0.10}\text{B}_{0.66}$ compositions reveal a significantly lower fracture resistance than the unalloyed coating, with values decreasing to $K_{IC} = 1.94 \pm 0.06$ and 1.69 ± 0.05 MPa $\sqrt{\text{m}}$, respectively (see Figure 8). In contrast, the maximum bending strain at failure remained comparable at $\epsilon \sim 1\%$ (see Figures 7b and c). The loss in as-deposited fracture toughness is attributed to the increasing presence of Si precipitates on the grain boundaries beyond an alloying content of 4 at.% – as previously revealed by detailed atom probe tomography [28] and in line with the hardness evolution (see Figure 3). Since these Si-enriched regions are not phase-pure, therefore contain additional contributions from the surrounding Cr-Si-B_{2±z} solid solution, good agreement is obtained in the RT fracture toughness located between the unalloyed $\text{Cr}_{0.28}\text{B}_{0.72}$ and fracture resistance of single crystal Si. Depending on the specimen size, the RT fracture toughness of pure Si is reported at $K_{IC} \sim 0.8\text{-}1.2$ MPa $\sqrt{\text{m}}$ [66,67].

Analogous to the $\text{Cr}_{0.28}\text{B}_{0.72}$ sample, increasing the temperature to $T = 400\text{ }^\circ\text{C}$ causes a decrease in fracture toughness of $\sim 0.4\text{ MPa}\sqrt{\text{m}}$ for both samples, while the maximum bending strain remained almost unaffected. However, continuing to $T = 600\text{ }^\circ\text{C}$ resulted in a significantly changed and highly interesting material response. Both Si containing samples showed drastically increased elastic deformability of the micro-cantilever, with ϵ approaching ~ 1.5 and $\sim 1.9\%$ for $\text{Cr}_{0.25}\text{Si}_{0.06}\text{B}_{0.69}$ and $\text{Cr}_{0.24}\text{Si}_{0.10}\text{B}_{0.66}$, respectively (see Figure 7b and c). Concomitantly, also the fracture resistance reveals an increase to $K_{IC} = 2.03 \pm 0.09$ and $1.61 \pm 0.07\text{ MPa}\sqrt{\text{m}}$, thus recovering close to the as-deposited values (see Figure 8). Moreover, the corresponding stress intensity - bending strain data highlights a slight curvature before failure – *i.e.*, deviating from a purely linear-elastic behavior – which suggests a temperature related onset of plastic deformation within the material. Consequently, it is important to note, that the actual fracture toughness may deviate slightly from the reported values, since the calculations were solely based on linear-elastic fracture theory.

At $T = 800\text{ }^\circ\text{C}$, severe plastic deformation is immediately noticeable in both Si-containing coatings upon cantilever loading (see Figure 7b and c). The actual fracture mode entirely changes from brittle cleavage fracture (see Figure 9, lower row), to a mechanism that results in extensive crack deflection and branching. SEM images of the open crack wake reveal splitting of the microstructure along column boundaries as well as distinct crack bridging ligaments throughout the cantilever cross-section (see Figure 10), pointing out the enhanced resistance to crack growth at elevated temperatures.

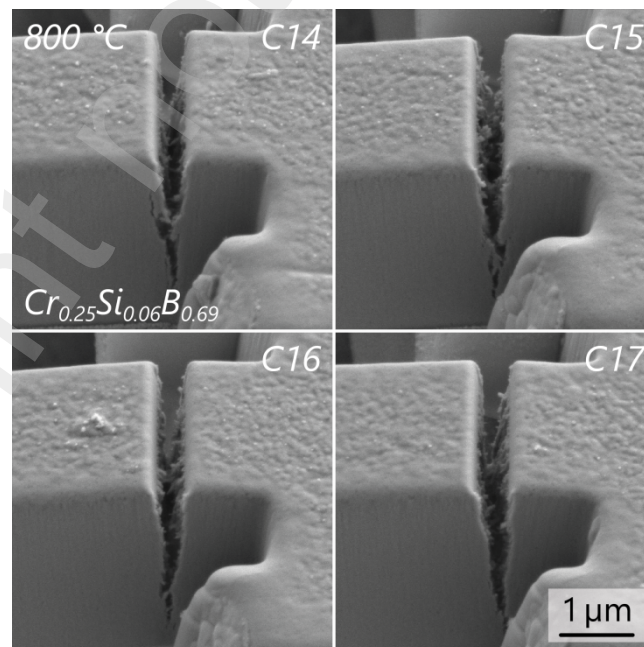


Figure 10: SEM images of the crack location for all cantilevers (C14-C17) tested at $T = 800\text{ }^\circ\text{C}$ on the $\text{Cr}_{0.25}\text{Si}_{0.06}\text{B}_{0.69}$ coating.

In fact, the fracture resistance increased to such an extent, that all cantilevers endured an extreme deflection of $\epsilon > 7\%$ (see inserts in Figures 7b and c), at which point the experiments were manually stopped. In this case, the authors refrain from reporting a single value for K_{Ic} (see arrows in Figure 8), since the calculated stress intensities are fully outside the boundaries given in Ref. [46]. However, presenting the load-displacement data in this normalized context provides a direct comparison to the curves recorded at lower temperatures. Moreover, since the cantilever cross-sections could not be evaluated – they were still attached to the base after the bending experiment – a mean value calculated from the geometries of samples fractured at lower temperatures was taken for reference.

With respect to temperature dependent structural evolution presented in Figure 6, a sequence of two successive mechanisms at $T = 600$ and $800\text{ }^\circ\text{C}$ is considered responsible for the fracture toughness development of the higher Si-containing coatings. Note, the samples were held at each temperature for several hours to reach thermal equilibrium prior to testing, thus all structural changes were able to attain the conditions presented in Figure 6. (i) At $T = 600\text{ }^\circ\text{C}$, both samples undergo enhanced segregation of pure Si from the Cr-Si-B_{2±z} solid solution towards the already Si-rich grain boundary sites. This increased occupation of the preferred crack pathways in combination with a brittle-to-ductile transition temperature (BDTT) of Si at $T \sim 600\text{ }^\circ\text{C}$, leads to the improved fracture toughness over $T = 400\text{ }^\circ\text{C}$ [66,68–70]. Although the fracture cross-sections appear straight without noticeable crack deflection (see Figure 9, lower row), the incorporation of this increasingly ductile phase between the Cr(-Si)-B_{2±z} matrix contributes to enhanced energy dissipation and possible crack arrest (see also the slight curvature of the $K_{Ic} - \epsilon$ data at $600\text{ }^\circ\text{C}$ in Figures 7b and c). (ii) At $T = 800\text{ }^\circ\text{C}$, Si segregation is well-advanced and the BDTT of Si is significantly exceeded. This causes the precipitates to provide the principal deformation regions during cantilever bending by enabling extensive plastic deformation. Furthermore, the weakly bound Si regions allow for crack branching by splitting of the microstructure along crystal columns as well as a crack bridging effect (see Figure 10). The mechanism also enables the vastly extended deformability of both specimen beyond the experimentally accessible range.

The fracture toughness of both samples was additionally evaluated at room temperature after the annealing treatment. A close matching value of $K_{Ic} \sim 1.65\text{ MPa}\sqrt{\text{m}}$ was obtained, irrespective of the overall Si composition (see Figure 8). This suggests, that once the thermally grown Si precipitates are embedded in the microstructure, they also dictate the room temperature fracture toughness below the BDTT of Si. In addition, the measured fracture toughness is close to the as-deposited value for the Cr_{0.24}Si_{0.10}B_{0.66} coating. This indicates an already enhanced presence of Si grain boundary decorations in the as-deposited state for the given composition.

4. Conclusion

This work investigates the effect of Si segregates and targeted synthesis variations on the structural evolution and mechanical properties of Si alloyed Cr-B_{2±z}-based thin films at ambient and elevated temperatures. Several AlB₂-structured Cr-Si-B_{2±z} thin films with Si concentrations up to 15 at.% were synthesized by DC magnetron sputtering and studied by RT nanoindentation as well as thermogravimetric analysis up to 1400 °C. Vacuum annealing treatments performed on coated Ti-6Al-4V up to 800 °C demonstrated the microstructural changes induced by thermally activated solid-state processes in the thin films as well as on the coatings-substrate interface. Complementary nanoindentation measurements provided details on the post-annealing hardness of these thin films. Moreover, the fracture resistance of selected Cr-Si-B_{2±z} compositions was studied by in-situ microcantilever bending experiments at temperatures up to 800 °C. The main findings are as follows:

- (1) An increased substrate bias of -120 V during film synthesis yields single-phased, B-overstoichiometric Cr-Si-B_{2±z} thin films with B/Cr ratios ranging from 2.6 to 2.8, irrespective of the Si concentration. The increased ion bombardment promotes the growth of mechanically superior, (001)-oriented coatings up to a Si concentration of 3 at.%. Enhanced film crystallinity is maintained up to 10 at.%, whereas higher concentrations promote grain refinement.
- (2) Highest RT hardness was obtained at $H \sim 30$ GPa for compositions with a Si content ≤ 3 at.%, beyond which a significant decrease towards $H \sim 20$ GPa is recorded. Concomitant with the change in preferred film orientation, the decrease coincides with a Si solubility limit at ~ 4 at.% within the Cr-Si-B_{2±z} solid solution, causing the formation of mechanically inferior Si-rich grain boundary precipitates. The corresponding Young's moduli were recorded in a range from $E \sim 340$ (Cr_{0.28}B_{0.72}), to 380 (Cr_{0.25}Si_{0.04}B_{0.71}), to 300 GPa (Cr_{0.23}Si_{0.15}B_{0.62}), respectively.
- (3) High temperature oxidation resistance up to 1400 °C was verified for all Cr-Si-B_{2±z} thin films with a Si content ≥ 8 at.%. The protective mechanism relies on the thermally activated precipitation of pure Si beyond 600 °C, coupled with the subsequent formation of a stable SiO₂-based scale. Contrary to the oxidation behavior of related binary TM-B₂, the oxidation protection was proven independent of the effective B/TM-ratio.
- (4) Despite revealing initial stages of recovery/recrystallisation between 600 and 800 °C, an unchanged film hardness was recorded for vacuum annealed Cr-Si-B_{2±z} compositions with a Si content below 10 at.%. Related to the oxidation protection mechanism, both Cr_{0.24}Si_{0.10}B_{0.66} and Cr_{0.23}Si_{0.15}B_{0.62} coatings obtain a surface hardness close to pure Si after annealing.
- (5) The increased contribution of mechanically weak Si-rich grain boundary regions with higher Si content resulted in decreasing RT fracture toughness, from $K_{IC} \sim 2.9$ MPa√m for Cr_{0.28}B_{0.72}, down to $K_{IC} \sim 1.7$ MPa√m for Cr_{0.24}Si_{0.10}B_{0.66}. After a slight decrease in fracture resistance between RT and

600 °C, a significantly improved high-temperature fracture toughness of $K_{IC} \sim 3.3$ MPa \sqrt{m} was recorded for the unalloyed Cr-B_{2+z}. Higher alloyed compositions revealed a similar behavior up to 400 °C, whereas at 800 °C Si-precipitation enabled high-temperature plasticity was observed. Surpassing the BDTT of Si introduced toughening mechanisms involving crack branching along column boundaries as well as crack bridging effects, resulting in a significantly improved fracture resistance.

Acknowledgments

The financial support by the Austrian Federal Ministry for Digital and Economic Affairs, the National Foundation for Research, Technology and Development and the Christian Doppler Research Association is gratefully acknowledged (Christian Doppler Laboratory "Surface Engineering of high-performance Components"). We also thank for the financial support of Plansee SE, Plansee Composite Materials GmbH, and Oerlikon Balzers, Oerlikon Surface Solutions AG. In addition, we want to thank the X-ray center (XRC) of TU Wien for beam time as well as the electron microscopy center - USTEM TU Wien - for providing the SEM and TEM facilities. The authors acknowledge TU Wien Bibliothek for financial support through its Open Access Funding Programme.

Data Availability Statement

The data that support the findings of this study are available from the corresponding author upon reasonable request.

Bibliography

- [1] M.E. Launey, R.O. Ritchie, *Adv. Mater.* 21 (2009) 2103–2110.
- [2] A.G. Evans, *J. Am. Ceram. Soc.* 73 (1990) 187–206.
- [3] R.O. Ritchie, C.J. Gilbert, J.M. McNaney, *Int. J. Solids Struct.* 37 (2000) 311–329.
- [4] R.O. Ritchie, *Nat. Mater.* 10 (2011) 817–822.
- [5] B. Gludovatz, R.O. Ritchie, *MRS Bull.* 47 (2022) 176–185.
- [6] X.J. Fan, R.T. Qu, Z.F. Zhang, *J. Mater. Sci. Technol.* 123 (2022) 70–77.
- [7] B. Gludovatz, A. Hohenwarter, D. Catoor, E.H. Chang, E.P. George, R.O. Ritchie,

- Science (80-). 345 (2014) 1153–1158.
- [8] Y. Mutoh, K. Ichikawa, K. Nagata, M. Takeuchi, J. Mater. Sci. 30 (1995) 770–775.
- [9] J. Xu, U. Ramamurty, E. Ma, JOM 62 (2010) 10–18.
- [10] Y. Wang, Y. Zhang, A. Godfrey, J. Kang, Y. Peng, T. Wang, N. Hansen, X. Huang, Commun. Mater. 2021 21 2 (2021) 1–10.
- [11] J.D. French, H.M. Chan, M.P. Harmer, G.A. Miller, J. Am. Ceram. Soc. 79 (1996) 58–64.
- [12] Q. Zhu, K. Shobu, J. Mater. Sci. Lett. 19 (2000) 1529–1531.
- [13] J. Shao, W. Li, H. Kou, Y. Deng, J. Am. Ceram. Soc. 105 (2022) 4348–4359.
- [14] J.A. Lemberg, M.R. Middlemas, T. Weingärtner, B. Gludovatz, J.K. Cochran, R.O. Ritchie, Intermetallics 20 (2012) 141–154.
- [15] H. Choe, D. Chen, J.H. Schneibel, R.O. Ritchie, Intermetallics 9 (2001) 319–329.
- [16] W.G. Fahrenholtz, G.E. Hilmas, I.G. Talmy, J.A. Zaykoski, J. Am. Ceram. Soc. 90 (2007) 1347–1364.
- [17] F. Monteverde, A. Bellosi, L. Scatteia, Mater. Sci. Eng. A 485 (2008) 415–421.
- [18] H. Deng, E.C. Dickey, Y. Paderno, V. Paderno, V. Filippov, A. Sayir, in: J. Mater. Sci., 2004, pp. 5987–5994.
- [19] W.G. Fahrenholtz, G.E. Hilmas, Scr. Mater. 129 (2017) 94–99.
- [20] C. Fuger, V. Moraes, R. Hahn, H. Bolvardi, P. Polcik, H. Riedl, P.H. Mayrhofer, MRS Commun. 9 (2019) 375–380.
- [21] W.G. Fahrenholtz, G.E. Hilmas, Int. Mater. Rev. 57 (2012) 61–72.
- [22] F. Monteverde, A. Bellosi, J. Electrochem. Soc. 150 (2003) B552.
- [23] F. Monteverde, L. Scatteia, J. Am. Ceram. Soc. 90 (2007) 1130–1138.
- [24] L. Silvestroni, K. Stricker, D. Sciti, H.J. Kleebe, Acta Mater. 151 (2018) 216–228.
- [25] I.G. Talmy, J.A. Zaykoski, M.M. Opeka, J. Am. Ceram. Soc. 91 (2008) 2250–2257.
- [26] T. Glechner, A. Bahr, R. Hahn, T. Wojcik, M. Heller, A. Kirnbauer, J. Ramm, S. Kolozsvári, P. Felfer, H. Riedl, Corros. Sci. 205 (2022) 110413.
- [27] T. Glechner, H.G. Oemer, T. Wojcik, M. Weiss, A. Limbeck, J. Ramm, P. Polcik, H. Riedl, Surf. Coatings Technol. 434 (2022) 128178.
- [28] L. Zauner, A. Steiner, T. Glechner, A. Bahr, B. Ott, R. Hahn, T. Wojcik, O. Hunold, J. Ramm, S. Kolozsvári, P. Polcik, P. Felfer, H. Riedl, SSRN Electron. J. (2022).
- [29] A.L. Chamberlain, W.G. Fahrenholtz, G.E. Hilmas, D.T. Ellerby, J. Am. Ceram. Soc. 87 (2004) 1170–1172.

- [30] F. Monteverde, S. Guicciardi, A. Bellosi, *Mater. Sci. Eng. A* 346 (2003) 310–319.
- [31] F. Monteverde, *Appl. Phys. A Mater. Sci. Process.* 82 (2006) 329–337.
- [32] A. Mège-Revil, P. Steyer, S. Cardinal, G. Thollet, C. Esnouf, P. Jacquot, B. Stauder, *Thin Solid Films* 518 (2010) 5932–5937.
- [33] M. Bartosik, R. Hahn, Z.L. Zhang, I. Ivanov, M. Arndt, P. Polcik, P.H. Mayrhofer, *Int. J. Refract. Met. Hard Mater.* 72 (2018) 78–82.
- [34] C. Fuger, R. Hahn, L. Zauner, T. Wojcik, M. Weiss, A. Limbeck, O. Hunold, P. Polcik, H. Riedl, *Mater. Res. Lett.* 10 (2022) 70–77.
- [35] J.M. Wheeler, R. Raghavan, V. Chawla, M. Morstein, J. Michler, *Surf. Coatings Technol.* 254 (2014) 382–387.
- [36] J.P. Best, J. Zechner, J.M. Wheeler, R. Schoepfner, M. Morstein, J. Michler, *Philos. Mag.* 96 (2016) 3552–3569.
- [37] J. Buchinger, L. Löfler, J. Ast, A. Wagner, Z. Chen, J. Michler, Z.L. Zhang, P.H. Mayrhofer, D. Holec, M. Bartosik, *Mater. Des.* 194 (2020).
- [38] A. Drnovšek, H.T. Vo, M.R. de Figueiredo, S. Kolozsvári, P. Hosemann, R. Franz, *Surf. Coatings Technol.* 409 (2021) 126909.
- [39] W.C. Oliver, G.M. Pharr, *J. Mater. Res.* 19 (2004) 3–20.
- [40] A.C. Fischer-Cripps, *Surf. Coatings Technol.* 200 (2006) 4153–4165.
- [41] G.C.A.M. Janssen, M.M. Abdalla, F. van Keulen, B.R. Pujada, B. van Venrooy, *Thin Solid Films* 517 (2009) 1858–1867.
- [42] G.G. Stoney, *Proc. R. Soc. A Math. Phys. Eng. Sci.* 82 (1909) 172–175.
- [43] D. Di Maio, S.G. Roberts, *J. Mater. Res.* 20 (2005) 299–302.
- [44] S. Brinckmann, K. Matoy, C. Kirchlechner, G. Dehm, *Acta Mater.* 136 (2017) 281–287.
- [45] J.M. Wheeler, P. Brodard, J. Michler, <https://doi.org/10.1080/14786435.2012.674647> 92 (2012) 3128–3141.
- [46] K. Matoy, H. Schönherr, T. Detzel, T. Schöberl, R. Pippan, C. Motz, G. Dehm, *Thin Solid Films* 518 (2009) 247–256.
- [47] J. Neidhardt, S. Mráz, J.M. Schneider, E. Strub, W. Bohne, B. Liedke, W. Möller, C. Mitterer, *J. Appl. Phys.* 104 (2008).
- [48] ICDD, Powder Diffr. File - Hexag. CrB₂ - 04-004-1734 (2011).
- [49] ICDD, Powder Diffr. File - Cubic Si - 00-027-1402 (2017).
- [50] C.L. Jiang, Z.L. Pei, Y.M. Liu, H. Lei, J. Gong, C. Sun, *Appl. Surf. Sci.* 288 (2014) 324–330.
- [51] H. Watanabe, N. Yamada, M. Okaji, *Int. J. Thermophys.* 25 (2004) 221–236.

- [52] Z. Nibennaoune, D. George, S. Ahzi, D. Ruch, Y. Remond, J.J. Gracio, *Thin Solid Films* 518 (2010) 3260–3266.
- [53] S. Dorri, J. Palisaitis, G. Greczynski, I. Petrov, J. Birch, L. Hultman, B. Bakhit, *Corros. Sci.* 206 (2022) 110493.
- [54] J. Thörnberg, B. Bakhit, J. Palisaitis, N. Hellgren, L. Hultman, G. Greczynski, P.O.Å. Persson, I. Petrov, J. Rosen, *Surf. Coatings Technol.* 420 (2021).
- [55] A.C. Fischer-Cripps, *Nanoindentation*, 3rd ed., Springer New York, New York, NY, 2011.
- [56] ICDD, Powder Diffr. File - Hexag. CrSi₂ - 04-001-7333 (2011).
- [57] ICDD, Powder Diffr. File - Orthorhombic CrB - 04-003-6125 (2011).
- [58] ICDD, Powder Diffr. File - Orthorhombic TiB - 04-005-6142 (2005).
- [59] ICDD, Powder Diffr. File - Alpha Titan. - 04-020-7055 (2016).
- [60] ICDD, Powder Diffr. File - Beta Titan. - 04-020-5 (2016).
- [61] L. Zauner, R. Hahn, E. Aschauer, T. Wojcik, A. Davydok, O. Hunold, P. Polcik, H. Riedl, *Acta Mater.* 239 (2022) 118260.
- [62] C. Fuger, R. Hahn, A. Hirle, P. Kutrowatz, M. Weiss, A. Limbeck, O. Hunold, P. Polcik, H. Riedl, *Surf. Coatings Technol.* (2022) 128806.
- [63] N.L. Okamoto, M. Kusakari, K. Tanaka, H. Inui, S. Otani, *Acta Mater.* 58 (2010) 76–84.
- [64] J.F. Li, R. Watanabe, *Mater. Trans. JIM* 40 (1999) 508–513.
- [65] C. Carry, A. Mocellin, *Ceram. Int.* 13 (1987) 89–98.
- [66] B.N. Jaya, J.M. Wheeler, J. Wehrs, J.P. Best, R. Soler, J. Michler, C. Kirchlechner, G. Dehm, *Nano Lett.* 16 (2016) 7597–7603.
- [67] I. Issa, C. Gammer, S. Kolitsch, A. Hohenwarther, P.J. Imrich, R. Pippan, D. Kiener, *Mater. Today* 48 (2021) 29–37.
- [68] D. Sen, C. Thaulow, S. V Schieffer, A. Cohen, M.J. Buehler, *Phys. Rev. Lett.* 104 (2010).
- [69] C. St. John, *Philos. Mag.* 32 (1975) 1193–1212.
- [70] E.D. Hintsala, S. Bhowmick, X. Yueyue, R. Ballarini, S.A.S. Asif, W.W. Gerberich, *Scr. Mater.* 130 (2017) 78–82.